

Single-Epoch Navigation Performance with Real BDS Triple-Frequency Pseudorange and EWL/WL Observations

Wang Gao¹, Chengfa Gao¹ and Shuguo Pan²

¹(School of Transportation, Southeast University, Nanjing, China)

²(School of Instrument Science and Engineering, Southeast University, Nanjing, China)
(E-mail: psg@seu.edu.cn)

Triple-frequency signals of China's BeiDou navigation satellite system (BDS) are now accessible in the Asia-Pacific region. It is well understood that the third frequency signal will improve the navigation performance. Some literatures have described several navigation methods by using triple-frequency signals, and evaluated the performance. However the experiments were mostly implemented on simulated or semi-simulated observations. In this paper we investigate the navigation performance using real BDS triple-frequency observations. Apart from the pseudorange observations, carrier observations are also used, since the extra-wide-lane and wide-lane ambiguities can be reliably resolved with a single epoch. Several single-epoch navigation methods using BDS triple-frequency observations are described and the corresponding navigation accuracy and reliability are assessed. Results show that P3 has the highest accuracy among the three pseudorange observations. For carriers, the wide-lane and extra-wide-lane observations can be used to obtain much higher navigation precision compared with pseudorange observations. Besides, the two ambiguity-fixed extra-wide-lane and wide-lane observations can also be combined to ionosphere-free form, which can still obtain sub-decimetre and decimetre navigation accuracy in horizontal and vertical directions respectively.

KEYWORDS

1. BeiDou navigation satellite system (BDS).
2. Single-epoch navigation.
3. Triple-frequency observations.
4. Positioning reliability.

Submitted: 20 September 2015. Accepted: 24 January 2016. First published online: 8 March 2016.

1. INTRODUCTION. Triple-frequency or multi-frequency Global Navigation Satellite Systems (GNSS) is the trend for almost all satellite systems, including the United States (US) modernised Global Positioning System (GPS), the Russian modernised Globalnaya Navigatsionnaya Sputnikovaya Sistema (GLONASS), the European Galileo system and the Chinese BeiDou System (BDS). At present, some GPS, GLONASS or Galileo satellites can already transmit real triple-frequency signals,

but there are only a small number of triple-frequency or multi-frequency satellites available. In contrast, there are 14 BDS satellites in orbit, which all transmit triple-frequency signals centred at B1 (1,561.098 MHz), B2 (1,207.140 MHz) and B3 (1,268.520 MHz). Extensive research has been done in the past 15 years to exploit the benefits from triple-frequency signals (Forssell et al., 1997; Vollath et al., 1999; Hatch et al., 2000; Teunissen et al., 2002; Richert and El-Sheimy, 2007; Feng, 2008; Li et al., 2010; Wang and Rothacher, 2013; Tang et al., 2014). These researches mainly focus on the utilisation of additional phase signal to speed up the integer Ambiguity Resolution (AR), especially for the Extra-Wide-Lane (EWL) or Wide-Lane (WL) ambiguities, which can be reliably fixed almost instantaneously. Although many researchers have proved that triple-frequency signals perform better than dual-frequency signals in narrow ambiguity resolution, however, instantaneous and reliable narrow ambiguity resolution is still a severe challenge for narrow-lane ambiguity resolution, especially for medium or long baselines (Li et al., 2010; Tang et al., 2014; Zhang and He, 2015; Gao et al., 2015).

On other hand, most GNSS users are in the navigation market for (sub) metre-level accuracy. Compared with centimetre-level accuracy, they prefer the faster (even instantaneous), more continuous and more reliable positioning or navigation service. Many researchers have studied using BDS, standalone or integrated, to obtain rapid centimetre-level positioning, even instantaneously for short baselines (Guo et al., 2011; Teunissen et al., 2014; Deng et al., 2014; He et al., 2014). However, as previously mentioned, instantaneous narrow-lane AR-based positioning is still a severe challenge for medium or long baselines, either with triple-frequency or dual-frequency signals. Some researchers also studied using pseudorange, EWL or WL observations from three frequency GNSS singles for real-time kinematic positioning, and the results have shown that sub-decimetre, decimetre or sub-metre positioning is feasible (Hernandez-Pajares et al., 2003; Feng and Li, 2010; Li et al., 2013). However most of these studies used only simulated data, which tends to produce optimistic results compared to using real observations. Now that the practical use of BDS triple-frequency observations is feasible, it is important to investigate its corresponding navigation performance and its benefit to users' decision-making. In this paper we will investigate single-epoch navigation performance using real BDS triple-frequency observations, especially the navigation performance using EWL and WL observations since the EWL and WL ambiguities can be resolved very reliably with a single epoch. Pseudorange precision and the single-epoch EWL and wide-lane WL AR are both analysed. Positioning accuracy and reliability in each single-epoch navigation model are identified.

The rest of this paper is organised as follows. Section 2 mainly introduces the basic observation equations and EWL/WL AR model for BDS. In Section 3 the noises of the three pseudoranges of BDS are analysed. Section 4 gives several single-epoch models using BDS triple-frequency observations. Then in Section 5, the experiments are carried out, which assess the single-epoch EWL/WL AR performance and positioning accuracy and reliability. Finally findings are summarised in Section 6.

2. FUNDAMENTAL EQUATIONS AND SINGLE-EPOCH EWL/WL AR MODEL.

2.1. *Basic Observation Equations and Definitions.* Without loss of simplicity, the combined Double-Difference (DD) carrier phase and pseudorange observation

equations in metres can be described as (Feng and Rizos, 2005; Urquhart, 2009; Li et al., 2010; Tang et al., 2014):

$$\Delta\phi_{(i,j,k)} = \Delta\rho + \Delta T - \eta_{(i,j,k)}\Delta I + \lambda_{(i,j,k)}\Delta N_{(i,j,k)} + \Delta\varepsilon_{\phi_{(i,j,k)}} \tag{1}$$

$$\Delta P_{[\alpha,\beta,\gamma]} = (\alpha + \beta + \gamma) \cdot (\Delta\rho + \Delta T) + \eta_{[\alpha,\beta,\gamma]}\Delta I_1 + \Delta\varepsilon_{P_{[\alpha,\beta,\gamma]}} \tag{2}$$

Where the combined DD carrier phase $\Delta\phi_{(i,j,k)}$ and pseudorange $\Delta P_{[\alpha,\beta,\gamma]}$ are defined

$$\Delta\phi_{(i,j,k)} = \frac{i \cdot f_1 \cdot \Delta\phi_1 + j \cdot f_2 \cdot \Delta\phi_2 + k \cdot f_3 \cdot \Delta\phi_3}{i \cdot f_1 + j \cdot f_2 + k \cdot f_3} \tag{3}$$

$$\Delta P_{[\alpha,\beta,\gamma]} = \alpha \cdot \Delta P_1 + \beta \cdot \Delta P_2 + \gamma \cdot \Delta P_3 \tag{4}$$

In Equations (1) to (4), Δ is the Double-Difference (DD, station- and satellite-difference) operator; the symbol ρ represents geometric distance from satellite to receiver; T is the tropospheric delay; I_1 is the first-order ionospheric delay on B1 carrier ('first-order' will be omitted for brevity of notation below); i, j, k are integer coefficients; $\Delta\phi_i$ and ΔP_i represents the DD carrier and pseudorange measurement in distance for the i th frequency of BDS; α, β, γ are arbitrary real numbers. The combined wavelength $\lambda_{(i,j,k)}$ and integer ambiguity $N_{(i,j,k)}$ are respectively defined as

$$\lambda_{(i,j,k)} = \frac{c}{i \cdot f_1 + j \cdot f_2 + k \cdot f_3} \tag{5}$$

$$N_{(i,j,k)} = i \cdot N_1 + j \cdot N_2 + k \cdot N_3 \tag{6}$$

The combined ionospheric scale factors, $\eta_{(i,j,k)}$ for carrier phase and $\eta_{[\alpha,\beta,\gamma]}$ for pseudorange are defined respectively as

$$\eta_{(i,j,k)} = \frac{f_1^2(i/f_1 + j/f_2 + k/f_3)}{f_{(i,j,k)}} \tag{7}$$

$$\eta_{[\alpha,\beta,\gamma]} = \alpha + \beta \cdot \frac{f_1^2}{f_2^2} + \gamma \cdot \frac{f_1^2}{f_3^2} \tag{8}$$

It is generally acknowledged that the three carrier measurements have the same precisions, i.e. $\sigma_{\Delta\phi_1} = \sigma_{\Delta\phi_2} = \sigma_{\Delta\phi_3} = \sigma_{\Delta\phi}$, so the variance of combined DD phase noise $\Delta\varepsilon_{\phi_{(i,j,k)}}$ is given as

$$\sigma_{\Delta\phi_{(i,j,k)}} = \frac{\sqrt{(i \cdot f_1)^2 + (j \cdot f_2)^2 + (k \cdot f_3)^2}}{f_{(i,j,k)}} \sigma_{\Delta\phi} = \mu_{(i,j,k)} \cdot \sigma_{\Delta\phi} \tag{9}$$

For the pseudoranges of BDS, the code chipping rate on B3 is ten times faster than those on B1 and B2, which means the noise of P3 is smaller than that of P1 and P2. Consider the differences in noise levels among P1, P2 and P3, the assumption for pseudorange noises $\Delta\varepsilon_{P_{[\alpha,\beta,\gamma]}}$ becomes

$$\sigma_{\Delta P_2} = q_1 \cdot \sigma_{\Delta P_1}, \quad \sigma_{\Delta P_3} = q_2 \cdot \sigma_{\Delta P_1} \tag{10}$$

so the variance of combined DD pseudorange noise is

$$\sigma_{\Delta P_{[\alpha,\beta,\gamma]}}^2 = \left[\alpha^2 + (q_1 \cdot \beta)^2 + (q_2 \cdot \beta)^2 \right] \cdot \sigma_{\Delta P_1}^2 = \mu_{[\alpha,\beta,\gamma]}^2 \cdot \sigma_{\Delta P_1}^2 \tag{11}$$

In Equation (9) and Equation (11), $\mu_{(i,j,k)}$ and $\mu_{[\alpha,\beta,\gamma]}$ represent the noise scale factor of $\Delta\phi_{(i,j,k)}$ and $\Delta P_{[\alpha,\beta,\gamma]}$ respectively.

2.2. *EWL and WL AR Models for BDS.* The resolution of BDS triple-frequency EWL and WL ambiguities has been verified to be easy and reliable (Tang et al., 2014; Zhao et al., 2015; Li et al., 2015). $\Delta N_{(0,-1,1)}$ and $\Delta N_{(1,-1,0)}$ are commonly recommended as the solved EWL and WL ambiguity of BDS respectively for medium baselines. The resolution models of $\Delta N_{(0,-1,1)}$ and $\Delta N_{(1,-1,0)}$ are directly given as Equation (12) and Equation (13), which are geometry-free and geometry-based respectively:

$$\Delta N_{(0,-1,1)} = \left[\frac{\Delta\phi_{(0,-1,1)} - \Delta P_{(0,1,1)}}{\lambda_{(0,-1,1)}} \right] \quad (12)$$

$$\begin{bmatrix} v'_{\text{EWL}(0,-1,1)} \\ v_{\text{WL}(1,-1,0)} \end{bmatrix} = \begin{bmatrix} B & 0 \\ B & I \cdot \lambda_{(1,-1,0)} \end{bmatrix} \begin{bmatrix} a \\ b \end{bmatrix} - \begin{bmatrix} l'_{\text{EWL}(0,-1,1)} \\ l_{\text{WL}(1,-1,0)} \end{bmatrix} \quad (13)$$

Where $[\cdot]$ in Equation (12) indicates the rounding operation. $\Delta P_{(0,1,1)}$ can be derived using the same form with Equation (3). The symbol $v'_{\text{EWL}(0,-1,1)}$ denotes the residual vector of ambiguity-fixed DD (0, -1,1) EWL carrier observations. $v_{\text{WL}(1,-1,0)}$ denotes the residual vector of DD (1, -1,0) WL carrier observations. I is the identity matrix. The unknown parameters a and b are the vectors of baseline components and the DD WL ambiguities, respectively. The last terms $l'_{\text{EWL}(0,-1,1)}$ and $l_{\text{WL}(1,-1,0)}$ are the Observed Minus Computed (OMC) vectors of the corresponding observations. The WL integer ambiguities estimated in Equation (13) can be searched and determined using the LAMBDA method (Teunissen, 1995). A note here is that the baselines used in the paper are medium baselines, so we allow the biased resolution caused by slight ionosphere delays since the WL observation has a long wavelength. The (1, -1,0) WL observation has much lower noise levels, so we fix the (1,-1,0) WL ambiguity with a geometry-based model to get a higher success rate. The PAF strategy will also be used to avoid the influence of ionospheric delay and guarantee the AR reliability. However, for long baselines, two EWL ambiguities are suggested (as in Li et al., 2015). Once the two EWL/WL ambiguities above are solved, we can fix any EWL/WL ambiguity, for instance, we can obtain $\Delta N_{(2,-1,-1)}$ by the equation

$$\Delta N_{(2,-1,-1)} = 2\Delta N_{(1,-1,0)} - \Delta N_{(0,-1,1)} \quad (14)$$

2.3. *Partial Ambiguity Fixing (PAF) Strategy.* In the WL ambiguity resolution described above, the extreme low-elevation satellites may still suffer from considerable atmospheric effects, the observation noises or others. It is therefore impossible to fix all ambiguities simultaneously at times. For this problem, (see Li et al., 2014), we introduce a PAF strategy with the ambiguity subset adaptively selected based on the successively increased elevations. From the procedures described in Section 2.2, we can get the float DD WL ambiguities together with their corresponding vc-matrix. We can divide the ambiguities into two parts, of which some are assumed to be able to be reliably fixed, and others are not or may not be fixed reliably. As shown in Equation (15), we suppose that \hat{N}_a , $Q_{\hat{N}_a}$ and \hat{N}_b , $Q_{\hat{N}_b}$ are the ambiguities and the corresponding vc-matrix of the two parts respectively

$$\begin{bmatrix} \hat{N}_a \\ \hat{N}_b \end{bmatrix} \cdots \cdots \begin{bmatrix} Q_{\hat{N}_a} & Q_{\hat{N}_a \hat{N}_b} \\ Q_{\hat{N}_b \hat{N}_a} & Q_{\hat{N}_b} \end{bmatrix} \quad (15)$$

If we can fix \hat{N}_a reliably and the number of ambiguities in \hat{N}_a is enough, we can use the

fixed ambiguities for positioning calculation. Of course we can also use the fixed ambiguities to improve the accuracies of the remaining ambiguities and their vc-matrix (Teunissen et al., 1999). In this paper we just consider the former, since the low-elevation ambiguities probably suffer more from the un-modelled atmospheric biases. The important thing is how to determine the subset. Here, we obtain the subset by the following steps:

Step (1): Sort the elevations of all satellites in an ascending order, and we can get a new elevation set such as Equation (16):

$$E = \{e_1, e_2, \dots, e_n | e_1 < e_2 < \dots < e_n\} \tag{16}$$

Where e_i represents the elevation at the i th order.

Step (2): Set the starting elevation for ambiguity selection (e_c) at e_1 , and we can obtain the subset $\hat{N}_a(e_1)$ and $Q_{\hat{N}_a}(e_1)$. Then the LAMBDA method is applied into the ambiguity search process. If the search results meet the following three conditions, the fixed ambiguities can be considered to pass the acceptance test and be introduced into the following positioning calculation.

- a) The bootstrapping AR success rate P_s , calculated according to Equation (17) from the decorrelated vc-matrix (Teunissen, 1998) is larger than the set threshold, P_0

$$P_s = \prod_{j=i}^n \left(2\Phi\left(\frac{1}{2\sigma_{z_{j|J}}}\right) - 1 \right) \tag{17}$$

Where $\Phi(x) = \int_{-\infty}^x \frac{1}{\sqrt{2\pi}} \exp\left\{-\frac{1}{2}v^2\right\} dv$ and $\sigma_{z_{j|J}} = (j = i, \dots, n, J = \{j + 1, \dots, n\})$ denote the conditional standard deviations of the decorrelated ambiguities.

- b) The ratio of the second minimum quadratic form of integer ambiguities residuals and the minimum one (Teunissen and Verhagen, 2009; Verhagen and Teunissen, 2013), which is shown in Equation (18), is larger than the set threshold, t_0

$$ratio = \frac{\|\hat{N}_a - \tilde{N}_{a2}\|_{Q_{\hat{N}_a}}}{\|\hat{N}_a - \tilde{N}_{a1}\|_{Q_{\hat{N}_a}}} \tag{18}$$

Where \tilde{N}_{a1} and \tilde{N}_{a2} are the ambiguity candidates with the minimum and second minimum quadratic form respectively; $\|\cdot\|_{Q_{\hat{N}_a}} = (\cdot)^T Q_{\hat{N}_a}^{-1} (\cdot)$.

- c) The number of ambiguities in the subset is larger than the set minimum threshold n_0 . This condition is set to ensure the selected satellites are sufficient to obtain reliable positioning results, since too few satellites are adverse to the positioning stability.

Step (3): If the conditions in Step (2) cannot be met, the starting elevation for ambiguity selection will be set at e_2 . Then Step (2) will be repeated. Of course if the starting elevation at e_2 is still unable to pass the acceptance test, the procedure will be continued with a larger starting elevation. But if it cannot meet the condition c)

in Step (2), the circulation will be stopped and the current epoch keeps the ambiguities floating.

In the experiments later in Section 5, P_0 is set at 0.95 considering the single-epoch mode; t_0 and n_0 are set at 3.0 and 5 respectively.

3. ANALYSIS OF BDS TRIPLE-FREQUENCY PSEUDORANGE NOISE. In order to investigate the precision differences among the three pseudoranges of BDS, we adopt an Epoch-Difference (ED) method to obtain the relative levels. Assuming that the change of ionospheric delays between the adjacent two epochs can be neglected and there are no cycle slips, the ED DD pseudorange observations are expected to be approximately the same with corresponding carrier observations similar in distance, since carrier observations have much smaller noise levels:

$$\text{Exp}(\Delta P_{i,t+1} - \Delta P_{i,t}) \approx \Delta \phi_{i,t+1} - \Delta \phi_{i,t} \quad (19)$$

Where $\text{Exp}(\cdot)$ represents the mathematical expectation. Considering that the carrier observations have much higher precision relative to pseudorange observations, the ED carrier observations can be treated as truth values. The pseudorange noises in ED form can be derived as

$$\varepsilon_{\Delta P_{i,(t,t+1)}} = \varepsilon_{\Delta P_{i,t+1}} - \varepsilon_{\Delta P_{i,t}} = \Delta \phi_{i,t+1} - \Delta \phi_{i,t} - (\Delta P_{i,t+1} - \Delta P_{i,t}) \quad (20)$$

Although the absolute pseudorange noises cannot be obtained directly, we can get the equivalent pseudorange precisions by using the law of error propagation

$$\sigma_{\Delta P_{i,(t,t+1)}}^2 = \sigma_{\Delta P_{i,t}}^2 + \sigma_{\Delta P_{i,t+1}}^2 - 2\rho_{\Delta P_{i,t}, \Delta P_{i,t+1}} \cdot \sigma_{\Delta P_{i,t}} \sigma_{\Delta P_{i,t+1}} \quad (21.1)$$

Where $\rho_{\Delta P_{i,t}, \Delta P_{i,t+1}}$ represents the time correlation of observations between two adjacent epochs. In Equation (21.1), we can assume $\sigma_{\Delta P_{i,t}} = \sigma_{\Delta P_{i,t+1}} = \sigma_{\Delta P_i}$, and when ignoring the time correlation, Equation (21.1) can be simplified as Equation (21.2)

$$\sigma_{\Delta P_{i,(t,t+1)}} = \sqrt{2}\sigma_{\Delta P_i} \quad (21.2)$$

In fact, the time correlation in Equation (21.1) of observations will have no influence on the calculation of ratios among the three pseudorange precisions which can be derived according to Equation (21.2). We calculate the actual results using a real baseline data with 51.9 km length, which contains BDS triple-frequency pseudorange and carrier observations. Figure 1 gives the ED pseudorange noises in the three frequencies from two BDS satellites, C02 and C14, as examples. We can see there exist obvious differences among the three pseudorange precisions. P3 has the highest precision, followed by P2, and P1 has the lowest precision. The Root Mean Square (RMS) values of all visible satellites in the period are calculated and shown in Figure 2, and the precision ratios between P2 and P1, P3 and P1 are shown in Figure 3. From Figures 2 and 3, we can see that although any two satellites have different RMS, there are still similar ratios between P2 and P1, or between P3 and P1 of all satellites. The mean values are 0.595 and 0.280 respectively, so the values q_1 and q_2 described in Section 2.1 will be assigned with these two values.

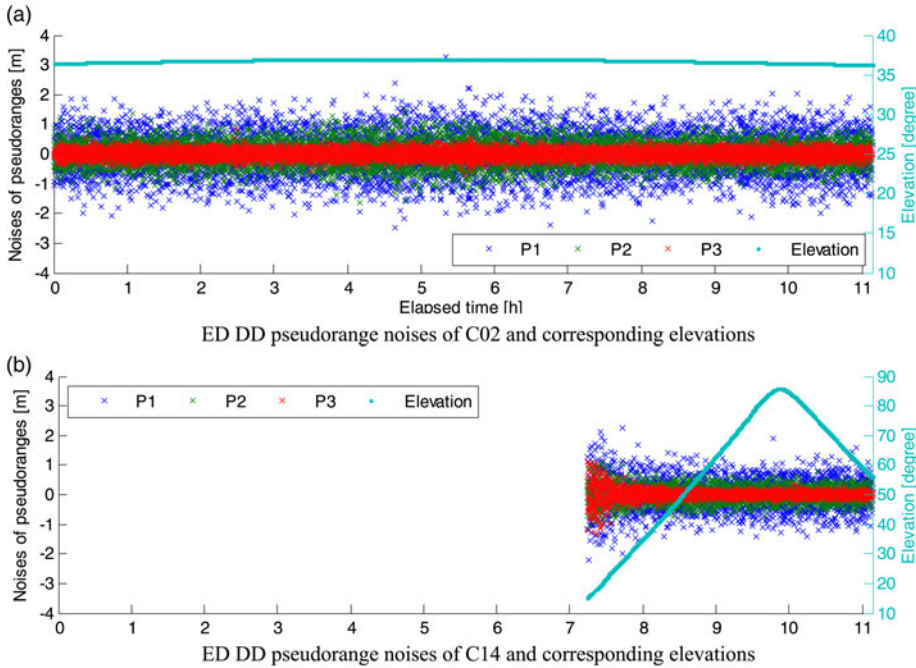


Figure 1. ED DD pseudorange noises of two BDS satellites.

4. POSITIONING MODELS USING BDS TRIPLE-FREQUENCY OBSERVATIONS. Using triple-frequency observations, we have more choices for single-epoch navigation. Besides the pseudorange observations, the ambiguity-fixed EWL and WL observations are also treated the same as pseudorange observations. According to whether the ionospheric effect is eliminated, we can divide these methods into two categories. One is the ionosphere-fixed model, which ignores the ionospheric effect and generally has smaller observation noise levels. The other is the ionosphere-float model, which eliminated the ionospheric effect by using the so-called ionosphere-free observations.

Category 1: Ionosphere-fixed model. The three pseudoranges can be used for positioning with a single-frequency model. The $(0, -1, 1)$ ambiguity can be resolved instantaneously and very reliably and then the ambiguity-fixed EWL observation $\Delta\phi_{(0,-1,1)}$ can also be used directly in positioning, with an ionospheric scale factor at -1.5915 , which is close to that in P3. However $\Delta\phi_{(0,-1,1)}$ has higher precision compared with any pseudorange. This is the significant advantage in the triple-frequency case. As described in Section 2.2, the ambiguity-fixed $\Delta\phi_{(0,-1,1)}$ can also be used to assist the resolution of $(1, -1, 0)$ WL ambiguity. The single-epoch $(1, -1, 0)$ WL AR may not be as reliable as the $(0, -1, 1)$ EWL AR, but once it passes the reliability test (e.g. the ratio test), we may get more precise observations. As stated before, when the two EWL/WL ambiguities above are solved, any EWL/WL ambiguity can be derived. Thus it needs to search for the optimal EWL or WL observation for better positioning. By setting the range $[-20, 20]$ for the combination coefficients i, j, k , we get the series of ionospheric scale factor $\eta_{(i,j,k)}$ and noise scale factor $\mu_{(i,j,k)}$ from all WL or EWL

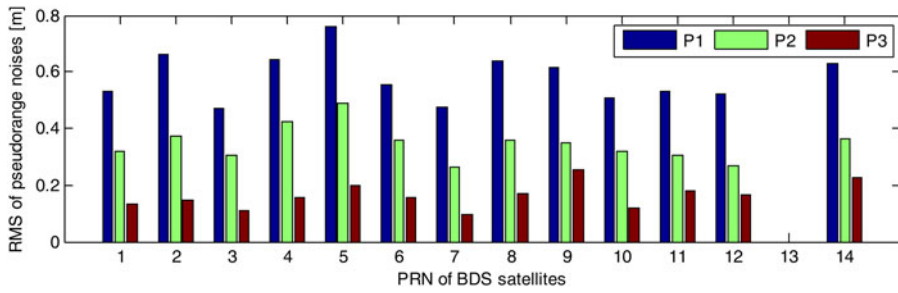


Figure 2. RMS of ED DD pseudorange noises of each satellite.

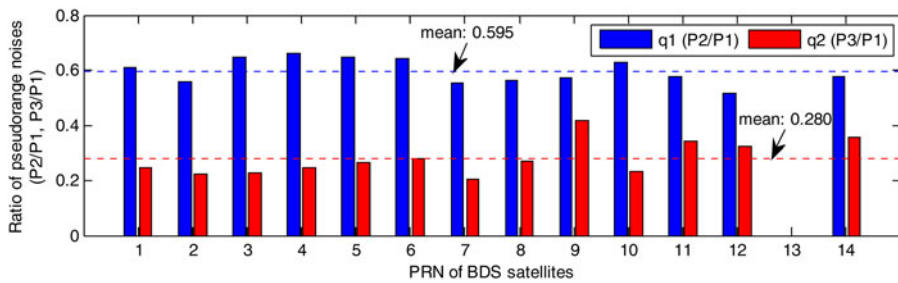


Figure 3. Ratios of pseudorange noises between P2 and P1, and between P3 and P1.

combinations, as are shown in Figure 4. We need to balance the ionospheric effects and the observation noises. However it is hard to make a decision as the ionospheric effects can hardly be foreseen. In this study, considering that the medium baseline is used, we prefer to consider the observation noises more. $\Delta\phi_{(2,-1,1)}$ is chosen here, related information of which can be seen in Table 1.

$$(i, j, k \in [-20, 20], i + j + k = 0)$$

Category 2: Ionosphere-float model. In the dual-frequency case, the ionosphere-free pseudorange can be combined to eliminate the ionospheric effect. In the triple-frequency case, the three pseudoranges can be combined together to obtain the optimal ionosphere-free pseudorange. This can be determined by the following equations (Gao et al., 2015; Zhao et al., 2015):

$$\begin{cases} \alpha + \beta + \gamma = 1 \\ \eta_{[\alpha, \beta, \gamma]} = \alpha + \beta \cdot \frac{f_1^2}{f_2^2} + \gamma \cdot \frac{f_1^2}{f_3^2} = 0 \\ \mu_{[\alpha, \beta, \gamma]}^2 = [\alpha^2 + (q_1 \cdot \beta)^2 + (q_1 \cdot \gamma)^2] \cdot \sigma_{\Delta P_1}^2 = \min \end{cases} \quad (22)$$

From Equation (22), we can obtain the coefficients α, β and γ by using the minimum-norm method to realise the minimum noise of the combined pseudorange. When we adopt $q_1 = 0.595$ and $q_2 = 0.280$, α, β and γ can be calculated as 2.3622, -1.8942

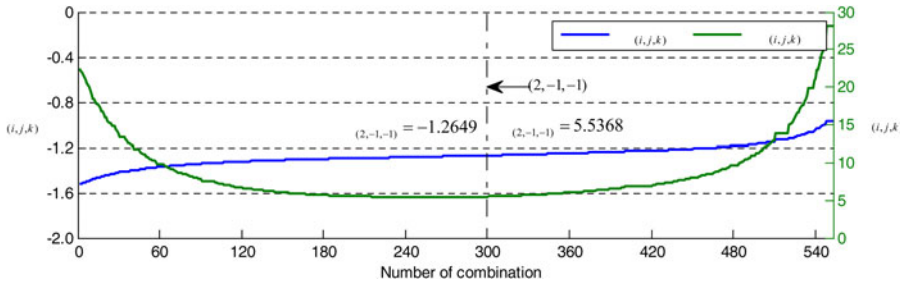


Figure 4. Ionospheric and noise scale factors from all WL or EWL combinations.

and 0.5320 respectively. Then the noise becomes $2.6215 \sigma_{\Delta P_1}$, which is slightly superior to that in the dual-frequency case (seen in Table 1).

Besides the pseudorange, if the WL ambiguities can be solved successfully, we can also use the ambiguity-fixed EWL and WL observations to combine the ionosphere-free carrier observation

$$\Delta\phi_{IF} = \left(\frac{\Delta\phi_{(1,-1,0)} - \lambda_{(1,-1,0)}\Delta N_{(1,-1,0)}}{\eta_{(1,-1,0)}} - \frac{\Delta\phi_{(0,-1,1)} - \lambda_{(0,-1,1)}\Delta N_{(0,-1,1)}}{\eta_{(0,-1,1)}} \right) / \left(\frac{1}{\eta_{(0,-1,1)}} - \frac{1}{\eta_{(1,-1,0)}} \right) \tag{23}$$

Then according to Equation (23), we can calculate the noise of the combined ionosphere-free carrier observation using Equation (24), and the precision can also be derived by using the law of error propagation, as Equation (25):

$$\varepsilon_{\Delta\phi_{IF}} = \frac{1}{f_1 - f_3} \cdot \left[\frac{f_1^2}{f_1 - f_2} \varepsilon_{\Delta\phi_1} - \left(\frac{f_1 f_2}{f_1 - f_2} - \frac{f_2 f_3}{f_3 - f_2} \right) \varepsilon_{\Delta\phi_2} - \frac{f_3^2}{f_3 - f_2} \varepsilon_{\Delta\phi_3} \right] \tag{24}$$

$$\sigma_{\Delta\phi_{IF}} = \frac{1}{f_1 - f_3} \cdot \sqrt{\left(\frac{f_1^2}{f_1 - f_2} \right)^2 + \left(\frac{f_1 f_2}{f_1 - f_2} - \frac{f_2 f_3}{f_3 - f_2} \right)^2 + \left(\frac{f_3^2}{f_3 - f_2} \right)^2} \cdot \sigma_{\Delta\phi} \tag{25}$$

The noise scale factor of $\Delta\phi_{IF}$ is 114.373 (seen in Table 1). One thing to note here is that the combinations using any two EWL/WL observations will lead to the same precision (Li et al., 2009; Feng and Li, 2010). The noises are further amplified, so the positioning using this observation suffers more from noise compared with the EWL and WL observations. However the remarkable advantage is that the ionospheric delay can be eliminated.

Table 1 summarises the positioning models with the various observations mentioned above. The effects of observation noises using the results in Figure 3 and ionospheric delays are also listed. The positioning performance using each kind of observation will be tested in detail in Section 5.

5. EXPERIMENTS AND ANALYSIS. In this section, we demonstrate navigation performance using BDS triple-frequency observations. The triple-frequency BDS data includes a 51.9 km baseline with 5 s sampling interval and a 45.1 km baseline with 15 s

Table 1. Observation and corresponding noise, ionospheric effect in each positioning model.

Positioning category	Observation	Precision	Ionospheric effect
Ionosphere-fixed model	P1	$\sigma_{\Delta P_1}$	$-\Delta I_1$
	P2	$0.595\sigma_{\Delta P_1}$	$-1.672\Delta I_1$
	P3	$0.280\sigma_{\Delta P_1}$	$-1.515\Delta I_1$
	EWL(0,-1,1)	$28.529\sigma_{\Delta\phi}$	$-1.592\Delta I_1$
	WL(2,-1,-1)	$5.537\sigma_{\Delta\phi}$	$-1.265\Delta I_1$
Ionosphere-float model	IF (P1,P2)	$2.6399\sigma_{\Delta P_1}$	0
	IF (P1,P2,P3)	$2.6215\sigma_{\Delta P_1}$	0
	IF (EWL,WL)	$114.373\sigma_{\Delta\phi}$	0

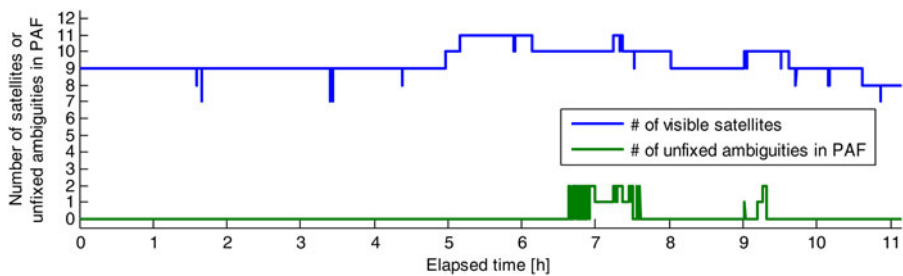


Figure 5. Number of visible satellites and the number of unfixed ambiguities in PAF.

sampling interval. The two baseline data lasted for about 11.1 h and 24 h respectively, and were all collected using the receivers produced by Shanghai Compass Navigation Co. Ltd. All the computations are implemented in single-epoch mode. For the 51.9 km baseline we will analyse the navigation performance with each model in Table 1 in detail. While for the 45.1 km baseline, we will directly give the statistical results of positioning since the two baselines have similar performance.

Firstly we investigate the results of the 51.9 km baseline. Figure 5 shows the number of visible satellites in the period and the number of unfixed ambiguities in PAF. We can see that for most of the time, there are still over seven satellites that can be used, even though 1–2 ambiguities cannot be fixed in PAF for some epochs. Figure 6 shows the Position Dilution Of Precision (PDOP) during the period. As we can see for most of the time, the PDOPs are between 2 and 4. The current BDS satellites mainly consist of GEO and IGSO satellites, so in China most visible satellites are in the southern part on the skyplot. As more MEO satellites are launched, the satellite geometry will no doubt become better.

We first investigate the single-epoch EWL and WL AR performance. Figure 7 shows the biases of single-epoch (0,-1,1) EWL AR. We can see all the biases are within ± 0.4 cycle with the RMS of 0.0648 cycle. Over 99.97% of the biases are in the ± 0.3 cycle region, so we can reliably resolve the (0,-1,1) ambiguities instantaneously. Also the (0,-1,1) EWL AR is baseline-length independent, since it has eliminated the tropospheric error, ionospheric error and orbital errors, etc. Figure 8 gives the ratios of WL AR both in FAF and PAF mode. For most of the time, we can directly get ratios larger than 3.0. However at some times, the ratios in PAF cannot reach the

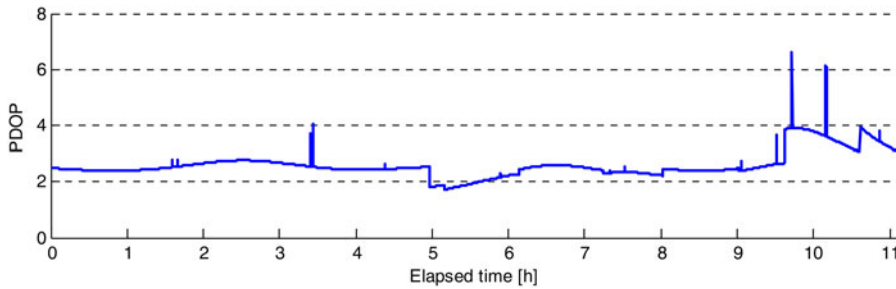


Figure 6. PDOP over the period.

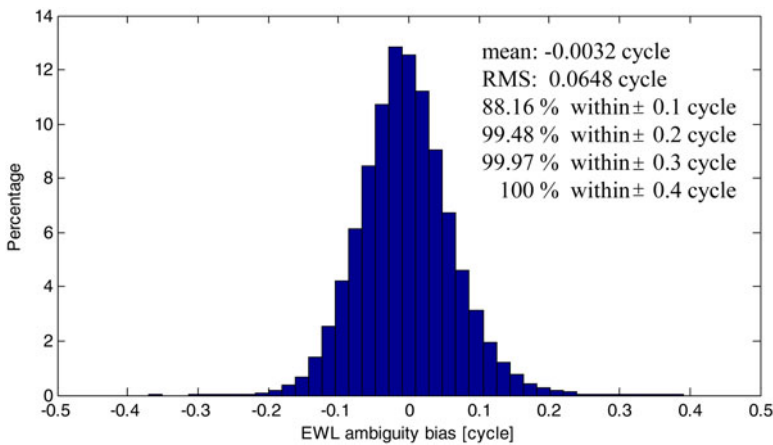


Figure 7. Results of (0,-1,1) EWL AR.

threshold, so we cannot decide whether the ambiguities are correct or not. This is mainly caused by low-elevation satellites, which suffer severely from atmospheric errors and high noise levels. After the PAF strategy is used, we can get the ideal ratios, since the ambiguity subset which can be fixed reliably is adaptively selected.

In the positioning aspect, we investigate the positioning performances using all the observations in Table 1. Figure 9 shows the horizontal and vertical positioning results using P1, P2 and P3 with the single-frequency mode. We can see, corresponding to the observation precisions, that the positioning results using the three pseudorange observations have obvious differences. The results using P3 have the smallest errors, followed by that using P2, and results using P1 have the largest errors. The statistics of the positioning results are listed in Table 2. It can be seen that for medium baselines, using single-frequency pseudorange observations, we can get sub-metre navigation performance in general (except in the up direction using P1).

Figure 10 shows the horizontal and vertical positioning results using (0,-1,1) EWL and (2,-1,-1) WL carrier observations. In these two models, the positioning results are much more concentrated when compared with those in pseudorange observations, since the observation noises are observably smaller. The ionospheric effects still

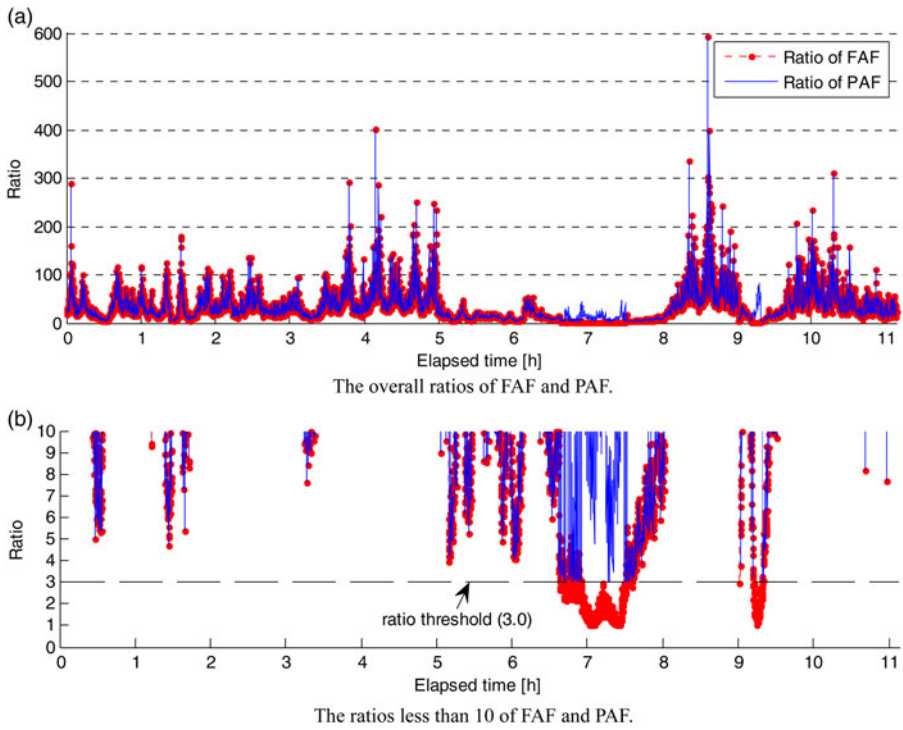


Figure 8. Ratios of (1,-1,0) WL AR.

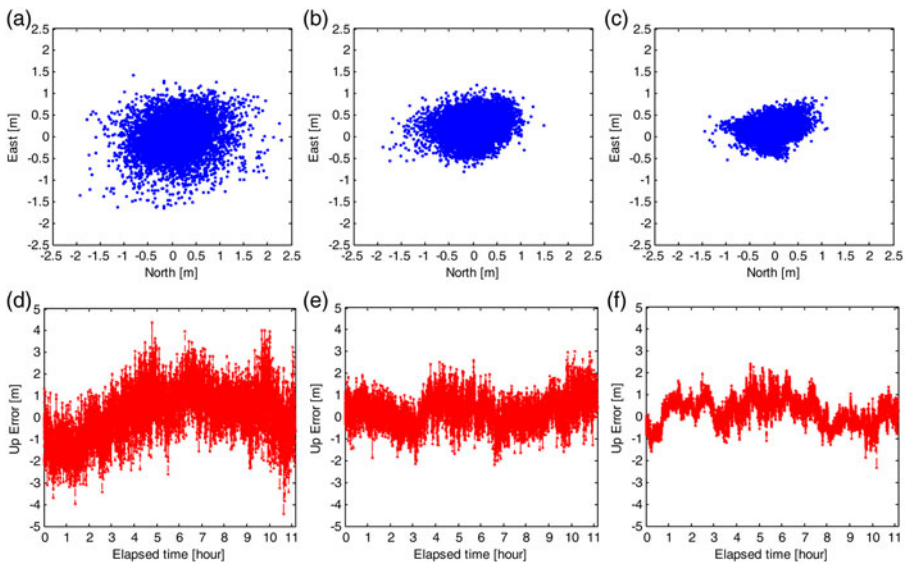


Figure 9. Positioning errors using P1, P2 and P3 with the single-frequency mode. (a) to (c) represent the scatter-plots of horizontal positioning errors using P1, P2 and P3 respectively. (d) to (f) represent the corresponding vertical positioning errors.

Table 2. Positioning results using each kind of observation of 51.9 km baseline.

	Mean (m)			RMS (m)		
	North	East	Up	North	East	Up
P1	0.0774	-0.0029	0.1235	0.4983	0.3992	1.2282
P2	0.0258	0.2564	0.2574	0.4024	0.3616	0.7390
P3	-0.0331	0.1999	0.2280	0.3115	0.2818	0.6610
EWL(0,-1,1)	-0.0585	-0.0313	0.2620	0.1249	0.0684	0.3307
WL(1,-1,0)	-0.0299	0.0349	0.1722	0.0554	0.0464	0.2076
IF (P1,P2)	0.1541	-0.3885	-0.0757	1.4242	1.2104	3.1825
IF (P1,P2,P3)	0.1450	-0.3880	-0.0696	1.4131	1.2105	3.1759
IF (EWL,WL)	0.0985	0.1594	-0.1428	0.3666	0.2701	0.6664

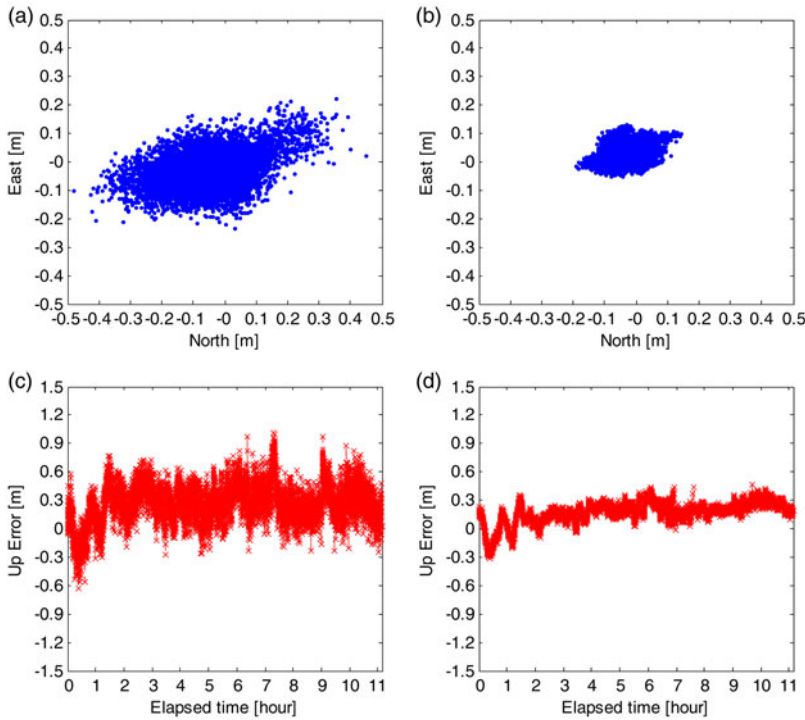


Figure 10. Positioning errors using EWL and WL observations. (a) and (b) respectively represent the scatter-plots of horizontal positioning errors using EWL and WL observations. (c) and (d) represent the corresponding vertical positioning errors.

exist, so we can see obvious biases in positioning results, especially in the vertical direction. From Table 2 we can see that decimetre and sub-decimetre horizontal positioning results can be obtained using (0,-1,1) EWL and (2,-1,-1) WL carrier observations respectively. In the vertical direction, decimetre-positioning performance can be obtained using both observations.

For long baselines, the ionospheric effects cannot be neglected. Figure 11 shows the performance of using the three kinds of ionosphere-free observations. From Table 1,

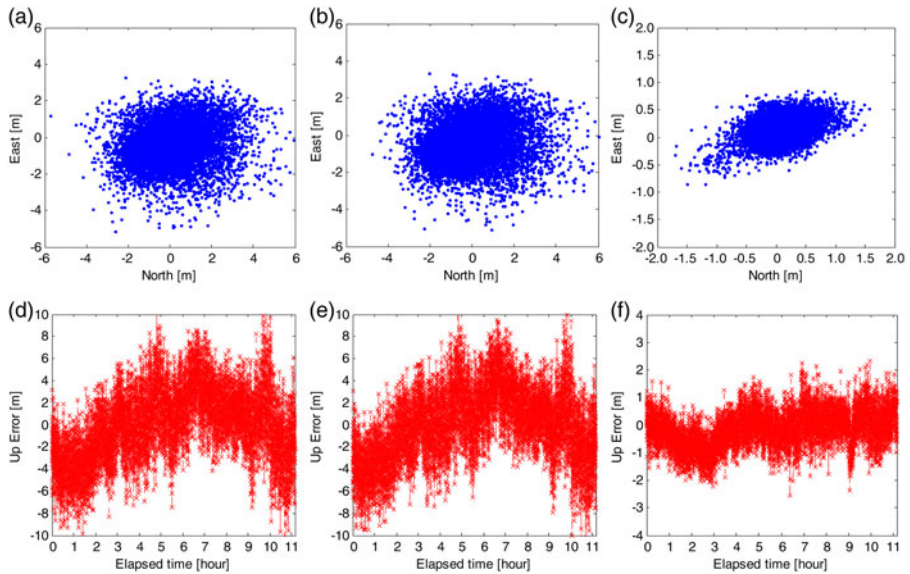


Figure 11. Positioning errors using the three ionosphere-free observations. (a) to (c) represent the scatter-plots of horizontal positioning errors using IF (P1,P2), IF (P1,P2,P3) and IF (EWL,WL) respectively. (d) to (f) represent the corresponding vertical positioning errors.

Table 3. Positioning results using EWL/WL observations of 45.1 km baseline.

	Mean (m)			RMS (m)		
	North	East	Up	North	East	Up
P1	-0.0243	0.0448	0.2406	0.4436	0.3558	1.0833
P2	-0.0464	0.0159	0.2539	0.3073	0.2790	0.7089
P3	-0.0834	-0.0711	0.1228	0.2373	0.1913	0.5269
EWL(0,-1,1)	-0.0636	-0.0283	0.0344	0.0950	0.0685	0.2037
WL(1,-1,0)	-0.0299	-0.0039	0.0121	0.0455	0.0243	0.1128
IF (P1,P2)	0.0084	0.0877	0.1549	1.1211	0.9317	2.7594
IF (P1,P2,P3)	-0.0140	0.0778	0.1528	1.1020	0.9260	2.7619
IF (EWL,WL)	0.1006	0.1077	-0.0619	0.2781	0.2456	0.6446

we know that the noises in IF (P1,P2) and IF (P1,P2,P3) have no apparent differences, so the positioning accuracies are similar. Also, the combination coefficient on P3 is just 0.5320, which is much smaller than that on P1 or P2, so the differences between the positioning errors using the two observations seems indistinct. As the observation noises of the two ionosphere-free pseudorange observation are amplified over 2.6 times, the influences of observation noises are much more serious compared with the single-frequency cases. As we can see from Table 2, the positioning accuracies in the three directions (north, east and up) are all worse than 1 m. So, although the ionospheric effects are eliminated, the ionosphere-free pseudorange observations are still not adoptable for single-epoch sub-metre navigation. Figure 11(c) and (f) gives the positioning errors using the ionosphere-free carrier observations combined by

ambiguity-fixed EWL and WL observations. We can see the positioning accuracies improve significantly when compared with using ionosphere-free pseudorange observations, to 0.3666 m, 0.2701 m and 0.6664 m in the three directions respectively. Although the noises are also amplified compared with (0,−1,1) EWL or (2,−1,−1) WL observations, decimetre to sub-metre navigation demand can still be satisfied. So it should be an ideal approach for the long-baseline cases, but one thing to note is that some seconds may be needed to obtain reliable WL ambiguities.

To be more convincing, the statistical results calculated from the 45.1 km baseline are also shown, as in Table 3. We can see the performance is consistent with that of the 51.9 km baseline in general, so it is not further analysed in this paper.

6. CONCLUSIONS. In this paper we have investigated single-epoch navigation performance using real BDS triple-frequency pseudorange and EWL/WL observations. Several single-epoch navigation models are described and the corresponding positioning precision and reliability are assessed. Based on the experimental results, we can conclude that P3 has the highest precision among the three pseudoranges of BDS, followed by P2 and P1 in order. For the medium baselines tested in the paper, when using the three pseudorange observations in single-frequency mode, sub-metre single-epoch navigation performances are obtained in general (except in the up direction using P1). We can also conclude that the (0,−1,1) EWL ambiguities can be reliably resolved instantaneously. So the ambiguity-fixed (0,−1,1) EWL observations can be directly used in position calculation. Single-epoch decimetre navigation performance is possible. Also, assisted by the ambiguity-fixed (0,−1,1) EWL observations and the PAF strategy, the WL ambiguities can also be resolved successfully within a single epoch for medium baselines. Using the optimal EWL/WL observations by balancing the ionospheric effects and noises, we can get better positioning results, even down to sub-decimetre in the horizontal direction.

The ionosphere-free pseudorange observations are very noisy, even for the optimal combination, so they are not adoptable for single-epoch sub-metre navigation. Although the noise of ionosphere-free carrier observations combined with ambiguity-fixed EWL and WL observations are also greatly amplified compared with (0,−1,1) EWL or (2,−1,−1) WL observations, decimetre to sub-metre navigation demand can still be satisfied. So it should be an ideal approach for long-baseline cases, but one thing to note is that several seconds may be needed to obtain the second reliable WL or EWL ambiguities.

Finally, we would point out that some numerical results in this paper are computed from the data used in the experiments, and there may be some differences from some other cases (e.g. for different receivers or different observation conditions). However, the general conclusions should be consistent.

ACKNOWLEDGEMENTS

The authors thank the anonymous reviewers for their valuable comments on the manuscript. This work was supported by the National Natural Science Foundation of China (Grant No. 41574026) and the Fundamental Research Funds for the Central Universities of China (Grant No. CXLX13_108).

REFERENCES

- Deng, C., Tang, W., Liu, J. and Shi, C. (2014). Reliable single-epoch ambiguity resolution for short baselines using combined GPS/BeiDou system. *GPS Solutions*, **18**(3), 375–386.
- Forsell, B., Martin-Neira, M. and Harrisz, R. A. (1997). Carrier phase ambiguity resolution in GNSS-2. In *Proceedings of the 10th International Technical Meeting of the Satellite Division of the Institute of Navigation (ION GPS 1997)*, 1727–1736.
- Feng, Y. and Rizos, C. (2005). Three carrier approaches for future global, regional and local GNSS positioning services: concepts and performance perspectives. In *Proceedings of ION GNSS 2005*, 2277–2787.
- Feng, Y. (2008). GNSS three carrier ambiguity resolution using ionosphere-reduced virtual signals. *Journal of Geodesy*, **82**(12), 847–862.
- Feng, Y. and Li, B. (2010). Wide area real time kinematic decimetre positioning with multiple carrier GNSS signals. *Science China Earth Sciences*, **53**(5), 731–740.
- Gao, W., Gao, C., Pan, S., Wang, D. and Wang, S. (2015). Single-epoch positioning method in network RTK with BDS triple-frequency widelane combinations. *Acta Geodaetica et Cartographica Sinica*, **44**(6), 641–648. (in Chinese with English abstract)
- Gao, W., Gao, C., Pan, S., Wang, D. and Deng, J. (2015). Improving Ambiguity Resolution for Medium Baselines Using Combined GPS and BDS Dual/Triple-Frequency Observations. *Sensors*, **15**(11), 27525–27542.
- Guo, H., He, H., Li, J. and Wang, A. (2011). Estimation and mitigation of the main errors for centimetre-level compass RTK solutions over medium-long baselines. *Journal of Navigation*, **64**(S1), S113–S126.
- Hatch, R., Jung, J., Enge, P. and Pervan, B. (2000). Civilian GPS: the benefits of three frequencies. *GPS Solutions*, **3**(4), 1–9.
- He, H., Li, J., Yang, Y., Xu, J., Guo, H. and Wang, A. (2014). Performance assessment of single-and dual-frequency BeiDou/GPS single-epoch kinematic positioning. *GPS Solutions*, **18**(3), 393–403.
- Hernández-Pajares, M., Zomoza, J. M. J., Subirana, J. S. and Colombo, O. L. (2003). Feasibility of wide-area subdecimeter navigation with GALILEO and modernized GPS. *Geoscience and Remote Sensing, IEEE Transactions on*, **41**(9), 2128–2131.
- Li, B., Shen, Y. and Zhang, X. (2009). Long-Range Real-Time Precise Navigation with Three Frequency GNSS. *Journal of Wuhan University (Natural Science Edition)*, **34**(7), 782–786. (in Chinese with English abstract)
- Li, B., Feng, Y. and Shen, Y. (2010). Three carrier ambiguity resolution: distance-independent performance demonstrated using semi-generated triple frequency GPS signals. *GPS Solutions*, **14**(2), 177–184.
- Li, B., Shen, Y. and Zhang, X. (2013). Three frequency GNSS navigation prospect demonstrated with semi-simulated data. *Advances in Space Research*, **51**(7), 1175–1185.
- Li, B., Shen, Y., Feng, Y., Gao, W., & Yang, L. (2014). GNSS ambiguity resolution with controllable failure rate for long baseline network RTK. *Journal of Geodesy*, **88**(2), 99–112.
- Li, B., Feng, Y., Gao, W. and Li, Z. (2015) Real-Time Kinematic Positioning Over Long Baselines Using Triple-Frequency BeiDou Signals. *IEEE Transactions on Aerospace and Electronic Systems*, DOI: 10.1109/TAES.2015.140643.
- Richert, T. and El-Sheimy, N. (2007). Optimal linear combinations of triple frequency carrier phase data from future global navigation satellite systems. *GPS Solutions*, **11**(1), 11–19.
- Tang, W., Deng, C., Shi, C. and Liu, J. (2014). Triple-frequency carrier ambiguity resolution for Beidou navigation satellite system. *GPS Solutions*, **18**(3), 335–344.
- Teunissen, P. J. G. (1995). The least-squares ambiguity decorrelation adjustment: a method for fast GPS integer ambiguity estimation. *Journal of Geodesy*, **70**(1–2), 65–82.
- Teunissen, P. J. G. (1998). Success probability of integer GPS ambiguity rounding and bootstrapping. *Journal of Geodesy*, **72**(10), 606–612.
- Teunissen, P. J. G., Joosten, P. and Tiberius, C. C. J. M. (1999). Geometry-free ambiguity success rates in case of partial fixing. In *Proceedings of ION-NTM 1999*, 25–27.
- Teunissen, P. J. G., Joosten, P. and Tiberius, C. C. J. M. (2002). A comparison of TCAR, CIR and LAMBDA GNSS ambiguity resolution. In *Proceedings of ION GPS 2002*, 2799–2808.
- Teunissen, P. J. G. and Verhagen, S. (2009). The GNSS ambiguity ratio-test revisited: a better way of using it. *Survey Review*, **41**(312), 138–151.
- Teunissen, P. J. G., Odolinski, R. and Odijk, D. (2014). Instantaneous BeiDou+ GPS RTK positioning with high cut-off elevation angles. *Journal of Geodesy*, **88**(4), 335–350.

- Urquhart, L. (2009). An analysis of multi-frequency carrier phase linear combinations for GNSS. *Senior technical report, Department of Geodesy and Geomatics Engineering Technical Report* (263).
- Verhagen, S. and Teunissen, P. J. (2013). The ratio test for future GNSS ambiguity resolution. *GPS Solutions*, **17**(4), 535–548.
- Vollath, U., Birnbach, S., Landau, L., Fraile-Ordoñez, J. M. and Martí-Neira, M. (1999). Analysis of Three-Carrier Ambiguity Resolution Technique for Precise Relative Positioning in GNSS-2. *Navigation*, **46**(1), 13–23.
- Wang, K. and Rothacher, M. (2013). Ambiguity resolution for triple-frequency geometry-free and ionosphere-free combination tested with real data. *Journal of Geodesy*, **87**(6), 539–553.
- Zhang, X. and He, X. (2015). Performance analysis of triple-frequency ambiguity resolution with BeiDou observations. *GPS Solutions*, DOI: 10.1007/s10291-014-0434-0.
- Zhao, Q., Dai, Z., Hu, Z., Sun, B., Shi, C. and Liu, J. (2015). Three-carrier ambiguity resolution using the modified TCAR method. *GPS Solutions*, **19**(4), 589–599.